CHEMISTRY OF MATERIALS

pubs.acs.org/cm

Article

Flux Crystal Growth of Ruddlesden–Popper Titanium Oxysulfides Li*Ln*TiO$_3$S (*Ln* = La–Gd): Lithium-Ion Mobility in Li$_{1-x}$Nd(Ti$_{1-x}$Nb$_x$)O$_3$S (*x* = 0–0.25)

Hongbo Yuan, Kaori Sugii, Gen Hasegawa, Yu Meng, Yoshitaka Matsushita, Hirofumi Akamatsu, Naoaki Kuwata,* Kazunari Yamaura, and Yoshihiro Tsujimoto*

Cite This: *Chem. Mater.* 2026, 38, 1457–1468

Read Online

ACCESS | Metrics & More | Article Recommendations | Supporting Information

ABSTRACT: We report the flux crystal growth of *n* = 1 Ruddlesden–Popper type titanium oxysulfides, Li*Ln*TiO$_3$S (*Ln* = La, Ce, Pr, Nd, Sm, Eu, Gd), using alkali metal halide molten salts. The transparent platelet Li*Ln*TiO$_3$S single crystals were pale yellow or orange, except for dark purple LiCeTiO$_3$S. All Li*Ln*TiO$_3$S members are stable in air, particularly up to 600 °C for *Ln* = Nd. Single crystal structure analysis revealed that Li*Ln*TiO$_3$S adopted a centrosymmetric tetragonal cell in the space group *P*4/*nmm* (no. 129) for *Ln* = La to Gd, which is in contrast to the corresponding oxide Li*Ln*TiO$_4$, which exhibits a structural symmetry lowering to *P*-42$_1$*m* for *Ln* = Sm–Dy via inversion symmetry breaking. The structure of Li*Ln*TiO$_3$S consists of single perovskite layers composed of corner-sharing TiO$_5$S octahedra, with (LiO)$_2$ antifluorite layers and (*Ln*S)$_2$ rock-salt layers stacked above and below along the *c*-axis. The lithium-ion conductivity of sintered polycrystalline LiNdTiO$_3$S was significantly enhanced by the substitution of Nb^{5+} for Ti^{4+}, which induced lithium vacancies. When *x* = 0.20, the bulk ionic conductivity increased from 3.00 × 10^{-7} S cm^{-1} at 25 °C to 1.46 × 10^{-2} S cm^{-1} at 500 °C, and the activation energy was 0.495 eV, which is lower than those of any other Ruddlesden–Popper type oxide-based solid electrolytes. Anion-directed material design using both oxide and sulfide ions provides opportunities for creating distinct classes of lithium-ion solid electrolytes.

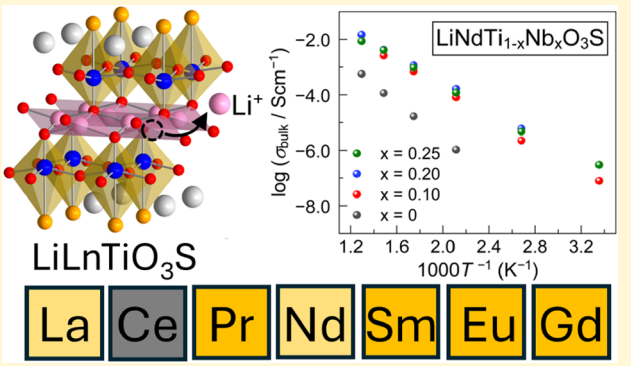

INTRODUCTION

The storage and conversion of renewable energy are crucial for addressing the challenges arising from the growing global reliance on fossil fuels. Lithium-ion batteries and storage devices are widely recognized as practical and efficient solutions and are extensively utilized in various applications. However, the current lithium-ion batteries may encounter challenges in satisfying the requirements of future large-scale energy storage systems owing to the flammable nature of conventional liquid organic electrolytes, which pose risks of leakage and combustion.[1] Given these safety concerns, there is an increasing acknowledgment of the necessity to develop inorganic all-solid-state Li-ion batteries that offer superior energy density, wide electrochemical window and temperature range, enhanced safety, and prolonged battery life.[2,3] However, in implementing inorganic solid electrolytes in all-solid-state batteries, solid electrolytes face various challenges, such as the stabilization of interfaces between electrolytes and electrodes, sustained physical contact among solid electrolyte particles, and inhibition of lithium dendrite growth on metal anodes. Among these criteria, the development of solid electrolytes that exhibit high ionic conductivity comparable to that of liquid electrolytes is particularly crucial. One such example is thio-LISICON-type Li$_{10}$GeP$_2$S$_{12}$ (LGPS),[4] which exhibits a high ionic conductivity of 12 × 10^{-3} S cm^{-1} at room temperature.[4] Since the discovery of this compound, several excellent sulfide-based ionic conductors, such as Li$_7$P$_3$S$_{11}$[5] and Li$_{3.25}$Ge$_{0.25}$P$_{0.75}$S$_4$,[6] have been identified. However, sulfide-based solid electrolytes are sensitive to moisture in the atmosphere and may release hydrogen sulfide, posing potential safety risks to all-solid-state batteries. In contrast, oxide-based solid electrolytes have lower ionic conductivity than sulfide-based electrolytes, but they offer superior stability in the atmosphere and at high temperatures. Among many types of promising oxide-based solid electrolytes,[7−10] *A*-site deficient perovskite-type lithium lanthanum titanate (La$_{2/3-x}$Li$_{3x}$TiO$_3$, LLTO) has been extensively investigated because of its high bulk conductivity of 1 × 10^{-3} S cm^{-1} and complex two-dimensional (2D) conduction via *A*-site vacant sites within

Received: October 31, 2025
Revised: January 13, 2026
Accepted: January 16, 2026
Published: January 22, 2026

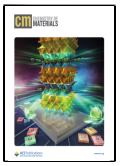

cuboctahedra.[11−15] Inspired by LLTO, in 2000, Tournoux et al. reported on the ion-conducting properties of n = 1 Ruddlesden−Popper (RP) type layered perovskite oxides LiLnTiO$_4$ (Ln = La, Nd).[16] The n is the number of perovskite layers. LiLnTiO$_4$ was synthesized via an ion-exchange reaction with analogous Na-substituted compounds,[17] resulting in a structure in which 2D perovskite layers composed of TiO$_6$ are sandwiched between antifluorite-type (LiO)$_2$ and rock-salt-type (LnO)$_2$ layers. The ionic conductivity of LiLaTiO$_4$ measured at 300 °C is on the order of 10^{-6} S cm^{-1}, while the ionic conductivity of the Ln = Nd phase is approximately 1 order of magnitude lower than that of LiLaTiO$_4$. The main reason for these low ionic conductivities is the absence of Li-ion defect sites, which restricts lithium-ion diffusion. In fact, Ramezanipour et al. have shown that n = 2 RP-type Li$_2$SrNb$_2$O$_7$[18] and n = 3 RP-type Li$_2$La$_2$Ti$_3$O$_{10}$[19] with similar (LiO)$_2$ layers, both with introduced lithium deficiencies, have total (= bulk and grain-boundary) conductivities more than 2 orders of magnitude higher than that of LiLaTiO$_4$. However, although several RP-type lithium-ion conductors have been reported to date, their bulk conductivities have not been characterized,[18−22] probably because of the nonuniform grain boundary characteristics of the electrolytes. This hinders the understanding of lithium-ion diffusion within the (LiO)$_2$ layers.

In our previous study, we discovered a layered oxysulfide, LiLa$_3$Ti$_2$S$_3$O$_6$, which contains Li atoms.[23] This oxysulfide can be regarded as a derivative of the n = 1 RP-type layered perovskite structure, consisting of perovskite layers composed of corrugated TiO$_5$S octahedra, LaS rock salt layers, and one-dimensional chains of LiO$_2$S$_2$ tetrahedra. We hypothesized that by transforming the coordination from LiO$_2$S$_2$ tetrahedra to LiO$_4$ tetrahedra, it might be possible to stabilize an antifluorite-type (LiO)$_2$ layer. In the course of exploring different types of RP-type oxysulfides, we successfully synthesized a series of n = 1 RP-type titanium oxysulfides, LiLnTiO$_3$S (Ln = La−Nd, Sm−Gd), by flux crystal growth and solid-state reaction methods. LiLnTiO$_3$S retains the space group $P4/nmm$ or flat perovskite layers for Ln = La−Gd, which differs from LiLnTiO$_4$, whose symmetry lowers to the noncentrosymmetric P-42$_1m$ for Ln = Sm−Dy,[24] involving oxygen octahedral rotation. We also observed a significant improvement in the ionic conductivity of LiNdTiO$_3$S via Ti-to-Nb substitution compared to related RP-type oxide-based electrolytes. LiNdTiO$_3$S serves as an ideal model compound for understanding lithium-ion diffusion within 2D (LiO)$_2$ antifluorite layers.

EXPERIMENTAL SECTION

Reagents

Li$_2$S (Sigma-Aldrich, 4N), Li$_2$O (Sigma-Aldrich, 4N), La$_2$S$_3$ (Kojundo Chemical Laboratory, 3N), La$_2$O$_3$ (Rare Metallic, 4N), Ce$_2$S$_3$ (Mitsuwa Chemicals, 3N), CeO$_2$ (Sigma-Aldrich, 3N), Ce (Sigma-Aldrich, 3N), Pr$_2$S$_3$ (Mitsuwa Chemicals, 3N), Pr$_6$O$_{11}$ (Wako Pure Chemical Industries, 3N), Nd$_2$S$_3$ (Mitsuwa Chemicals, 3N), Nd$_2$O$_3$ (Rare Metallic, 3N), Nb$_2$O$_5$ (Rare Metallic, 3N), Sm$_2$S$_3$ (Kojundo Chemical Laboratory, 3N), Sm$_2$O$_3$ (Rare Metallic, 3N), EuS (Mitsuwa Chemicals, 3N), Eu$_2$O$_3$ (Sigma-Aldrich, 4N), Gd$_2$S$_3$ (Mitsuwa Chemicals, 3N), Gd$_2$O$_3$ (Rare Metallic, 3N), and TiO$_2$ (Rare Metallic, 4N) powders were used as received. KI (Sigma-Aldrich, 2N) and CsCl (Sigma-Aldrich, 3N) were heated at 260 °C prior to use. All raw materials were stored in an argon-filled glovebox (moisture and oxygen levels less than 0.1 ppm), and all manipulations before starting the reactions were performed in a glovebox or under vacuum.

Crystal Growth and Elemental Analysis

Single crystals of LiLnTiO$_3$S (Ln = La, Ce, Pr, Nd, Sm, Eu, Gd) were obtained by the flux growth method using KI (for Ln = La, Nd, Eu) or CsCl (for Ln = Ce, Pr, Sm, Gd) as a molten solvent. For Ln = La, 0.5 mmol of Li$_2$S, 0.5 mmol of La$_2$S$_3$, 1 mmol of TiO$_2$, and 4.75 mmol of KI were combined. One mmol of Li$_2$S, 0.5 mmol of Ln_2S$_3$, 1 mmol of TiO$_2$, and 4.75 mmol of KI for Ln = Nd and CsCl for Ln = Ce, Pr and Sm were combined. One mmol of Li$_2$S, 0.5 mmol of Ln_2O$_3$, 1 mmol of TiO$_2$, and 4.75 mmol of KI for Ln = Eu and CsCl for Ln = Gd were combined. Each mixture was loaded into an alumina crucible and flame-sealed in fused silica tubes under a vacuum of 1 Pa. Single crystals of a 10% lithium-deficient phase, Li$_{0.9}$NdTi$_{0.9}$Nb$_{0.1}$O$_3$S, were grown from molten KI salt. 0.9 mmol of Li$_2$S, 0.5 mmol of Nd$_2$S$_3$, 0.05 mmol of Nb$_2$O$_5$, 0.9 mmol of TiO$_2$, and 4.75 mmol of KI were loaded into an alumina crucible and flame-sealed in a fused silica tube under a vacuum of 1 Pa. All starting materials were heated in muffle furnaces to 850 °C at 2.29 °C/min, held for 24h, cooled to 550 °C at 0.08 °C/min, and finally naturally cooled to room temperature by turning off the furnaces. The products were then washed with sonicated water to remove the flux. Rectangular-shaped crystals of LiLnTiO$_3$S (Ln = La, Ce, Pr, Nd, Sm, Eu, Gd) and Li$_{0.9}$NdTi$_{0.9}$Nb$_{0.1}$O$_3$S, which were pale yellow to orange in color except for dark purple in the Ln = Ce phase, were collected via vacuum filtration (Figure 1). Typical dimensions of these single crystals

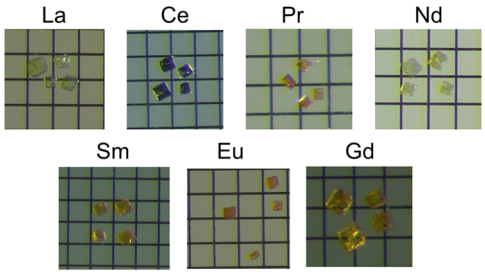

Figure 1. Photographs of LiLnTiO$_3$S (Ln = La, Ce, Pr, Nd, Sm, Eu, Gd) single crystals on a 0.1 mm-grid glass plate.

were approximately 0.05 × 0.05 × 0.02 mm^3. Elemental analysis of the single crystals was performed using a scanning electron microscope (SEM, HITACHI-TM3000) equipped with an energy dispersive X-ray (EDX) spectrometer (Oxford Instruments, Swift ED3000) (Figure S1). The accelerating voltage was set to 15 kV. EDX analysis indicated Ln:Ti:S atomic ratio of approximately 1:1:1 for LiLnTiO$_3$S and Nd:Ti:Nb:S atomic ratio of 1:0.9:0.1:1 for Li$_{0.9}$NdTi$_{0.9}$Nb$_{0.1}$O$_3$S, respectively, which were in good agreement with the chemical compositions determined by single-crystal structure analysis. To quantitatively analyze the content of Li atom, an inductively coupled plasma-optical emission spectrometry (ICP-OES, Agilent 5800) measurements were performed for LiNdTiO$_3$S as a representative. The mass ratio of Li:Nd:Ti was 2.228(2):51.27(3):16.72(3), which is also consistent with the results of EDX and single-crystal structure analysis.

Single Crystal Structure Determination

Single crystal X-ray diffraction data of LiLnTiO$_3$S (Ln = La, Ce, Pr, Nd, Sm, Eu, Gd) and Li$_{0.9}$NdTi$_{0.9}$Nb$_{0.1}$O$_3$S were collected using a Rigaku XtaLAB mini II diffractometer (Mo Kα radiation) at room temperature. Data collection covered 98% of the reciprocal space to $2\theta_{max}$ = 61.2° with R_{int} = 4.73%, 5.23%, 3.17%, 3.84%, 4.00%, 3.90%, 4.53% and 5.59% of LiLnTiO$_3$S (Ln = La, Ce, Pr, Nd, Sm, Eu, Gd) and Li$_{0.9}$NdTi$_{0.9}$Nb$_{0.1}$O$_3$S, respectively, after absorption correction. The crystal structures were solved using a dual-space algorithm (SHELXT)[25] and refined using a full-matrix least-squares method with SHELXL[26] using an Olex2 graphical user interface.[27]

Solid State Reaction

Polycrystalline powder samples of LiLnTiO$_3$S (Ln = La, Ce, Pr, Nd, Sm, Eu, Gd) and Li$_{1-x}$Nd(Ti$_{1-x}$Nb$_x$)O$_3$S (x = 0, 0.10, 0.20, 0.25, 0.30, 0.40) were synthesized by using a stoichiometric ratio of the following

https://doi.org/10.1021/acs.chemmater.5c02924
Chem. Mater. 2026, 38, 1457−1468

starting materials except lithium rich condition for *Ln* = Eu, (a) Li_2S, La_2O_3, La_2S_3, and TiO_2, (b) Li_2S, CeO_2, Ce_2S_3, Ce and TiO_2 (c) Li_2S, Pr_6O_{11}, Pr_2S_3, and TiO_2, (d) Li_2S, Nd_2O_3, Nd_2S_3, and TiO_2, (e) Li_2S, Nd_2O_3, Nd_2S_3, and Nb_2O_5, TiO_2, (f) Li_2S, Sm_2O_3, Sm_2S_3, and TiO_2, (g) Li_2O, EuS, and TiO_2, (h) Li_2S, Gd_2O_3, Gd_2S_3, and TiO_2. Each mixture was ground thoroughly with an agate mortar and pestle, pressed into a pellet, sealed in a fused silica tube under a vacuum of 1 Pa, and then heated in a muffle furnace at temperatures ranging from 900 to 1000 °C for 24 h.

Powder XRD, Thermogravimetric–Differential Thermal Analysis (TG-DTA), and UV–vis–NIR Reflectance Spectroscopy

Powder XRD patterns of Li*Ln*TiO_3S (*Ln* = La, Ce, Pr, Nd, Sm, Eu, Gd) and $Li_{1-x}Nd(Ti_{1-x}Nb_x)O_3S$ (x = 0, 0.10, 0.20, 0.25, 0.30, 0.40) were collected using a Rigaku MiniFlex-600 diffractometer (Cu Kα radiation) in the 2θ range of 5–70° with a step of 0.02° at room temperature. Thermogravimetric–differential thermal analysis (TG-DTA) of the $LiNdTiO_3S$ powder samples was performed using a Rigaku TG-DTA8188 system under flowing N_2 or O_2 atmosphere (1.0 L/min). The sample was loaded into an alumina crucible and heated to 1000 °C at 10 °C/min. The UV–vis–NIR reflectance spectra of Li*Ln*TiO_3S powder samples were collected using a Shimadzu UV-2600 UV–vis–NIR spectrometer (used in the diffuse reflectance mode) equipped with an integrating sphere in the range of 220–1200 nm. Deuterium and halogen lamps were used as sources of UV and visible-NIR light, respectively. The recorded reflectance spectra were converted into absorption data using the Kubelka–Munk function.

Electrochemical Impedance Spectroscopy (EIS) Measurements

$Li_{1-x}Nd(Ti_{1-x}Nb_x)O_3S$ (x = 0, 0.10, 0.20, 0.25) powder samples, which were synthesized as described above, were pelletized by pressing at 100 kN with a diameter and thickness of 10 and 1 mm, respectively, followed by a second sintering in an evacuated fused silica tube under the same heating conditions. The pellets were then polished with waterproof abrasive papers to a thickness of less than 0.6 mm. The densities of the pellets at x = 0, 0.10, 0.20, and 0.25, which were measured with a vernier caliper are 3.791(4), 3.664(4), 3.558(4), and 3.676(3) g/cm^3, respectively, which are approximately relative densities of approximately 75%. These low sintered densities are attributed to the presence of numerous pores formed within the pellets, as evidenced by the SEM observations (S-4300, Hitachi Ltd.), irrespective of Nb doping (Figure S2). Both the top and bottom sides of the pellets were sputtered with gold as the electrodes using an ion coater (Quick Coater, SC-701 MkII Advance). The ionic conductivities of $Li_{1-x}Nd(Ti_{1-x}Nb_x)O_3S$ were measured via EIS using a high-frequency impedance test system (HT-Z2-HF, TOYO) equipped with an impedance analyzer (E4990A, KEYSIGHT) in the frequency and temperature ranges of 20 Hz to 100 MHz and 25–500 °C in air at an AC amplitude voltage of 10 mV. The activation energy (E_a) of ac conductivity (σ) was calculated using the Arrhenius equation

$$\sigma T = \sigma_0 \cdot \exp(-E_a/k_B T) \quad (1)$$

where T, σ_0, and k_B are the absolute temperature, pre-exponential factor, and Boltzmann constant, respectively.

Density Functional Theory (DFT) Calculations

First-principles DFT calculations were performed on $LiLaTiO_3S$ using the CASTEP software.[28] Projector augmented-wave potentials were used for the Li, La, Ti, O, and S atoms. The cell parameters and atomic positions were optimized based on the experimentally determined crystal structure until the maximum force on each atom was less than 0.02 eV/Å, followed by band structure and density of states (DOS) calculations. Plane wave basis sets with a cutoff energy of 620 eV were used for the calculations. The self-consistent field tolerance was 1.0×10^{-6} eV/atom, and the k-point mesh was 6 × 6 × 2.

To investigate the structural instability, phonon band structures were calculated for $LiLaTiO_3S$ and $LiGdTiO_3S$ using a finite-displacement supercell approach, as implemented in the PHONOPY code.[29,30] Force constant matrices were computed using the PBE-GGA functional and VASP code[31,32] for the optimized structures. Phonon band structures were depicted in the first Brillouin zone using the sumo-bandplot program.[33]

Bond-Valence-Based Energy Calculations

The bond-valence-based energy (BVE)[34−36] of a test lithium ion (Li^+) in the crystal structure of $LiNdTiO_3S$ was obtained with the SoftBV program[36] to study the lithium-ion migration paths. The BVE landscape was calculated with a spatial resolution of approximately 0.1 Å using the crystal structure determined by single crystal structure analysis. The BVE landscape was drawn with VESTA.[37]

RESULTS

Flux Crystal Growth

The discoveries of Li*Ln*TiO_3S (*Ln* = La–Nd, Sm–Gd) result from the identification of square-shaped crystals of $LiLaTiO_3S$ as a minor byproduct of the KI flux method that produced rod-shaped crystals of $LiLa_3Ti_2S_3O_6$. Therefore, similar flux method using KI was applied to single crystal growth of all present members other than $LiLaTiO_3S$, resulting in successful growth of only the *Ln* = La, Nd, and Eu single crystals. In contrast, the growth of single crystals of *Ln* = Ce, Pr, Sm, and Gd was achieved by using CsCl. In all these reactions, single crystals of byproducts such as simple oxides and/or sulfides were also formed, making it impossible to isolate the Li*Ln*TiO_3S crystals and difficult to estimate the product yield.

Crystal Structure of Li*Ln*TiO_3S

Single-crystal structure analysis revealed that Li*Ln*TiO_3S adopted a primitive tetragonal cell in the space group *P*4/*nmm* (no.129). The asymmetric unit contained one Li atom at the Wycoff position 2*b*, one *Ln* atom at 2*c*, one Ti atom at 2*c*, one S atom at 2*c*, one O1 atom at 4*f* (equatorial site), and one O2 atom at 2*c* (apical site). The details of the structural refinement are listed in Table S1. The atomic coordinates and equivalent displacement parameters are listed in Tables S2–S8, and the anisotropic displacement parameters are listed in Tables S9–S15. A schematic of the crystal structure of Li*Ln*TiO_3S is shown in Figure 2, and the lattice parameters and unit cell volumes in Figure 3. Selected interatomic distances and angles are summarized in Figure 4 and Tables S16–S22.

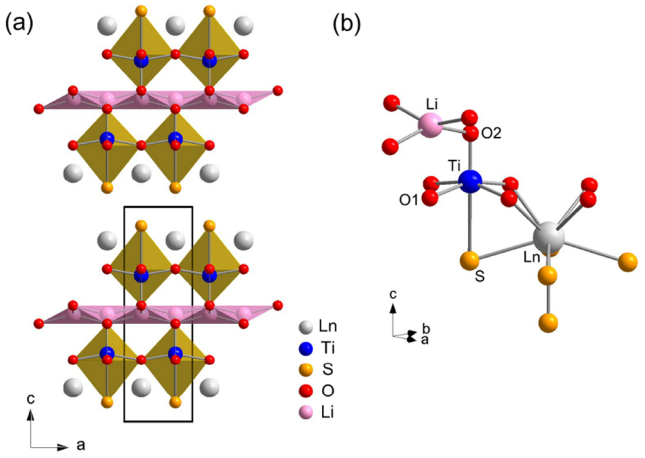

Figure 2. Schematic views of (a) the crystal structure of Li*Ln*TiO_3S and (b) local coordination environments around metal centers. Gray, blue, pink, yellow, and red spheres stand for *Ln*, Ti, Li, S, and O atoms, respectively.

https://doi.org/10.1021/acs.chemmater.5c02924
Chem. Mater. 2026, 38, 1457−1468

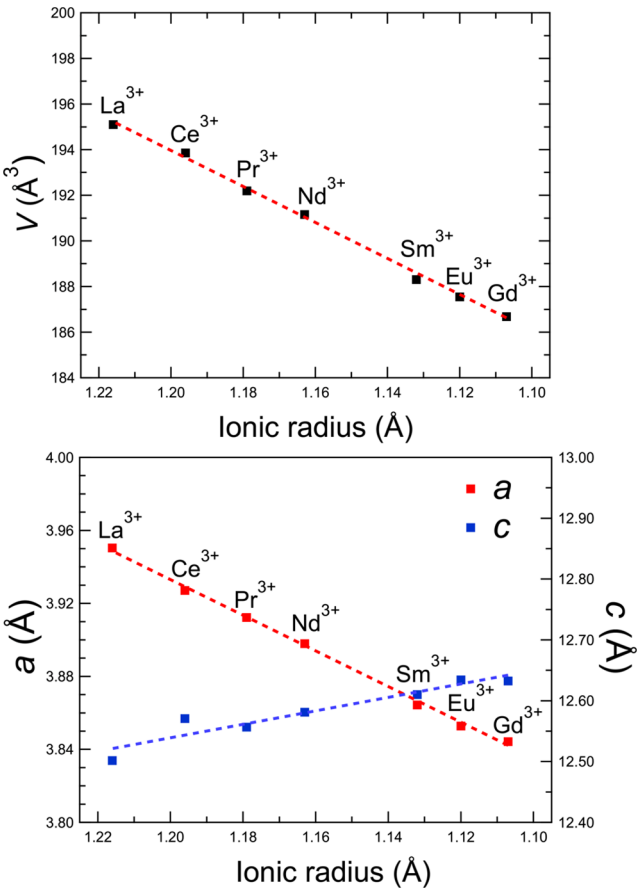

Figure 3. Lattice parameters and volume of Li*Ln*TiO_3S single crystals as a function of ionic radius of Ln^{3+}.

Li*Ln*TiO_3S is isostructural with $LiLaTiO_4$ with the $n = 1$ RP-type structure. Li*Ln*TiO_3S shows not only layered ordering of *A*-site cations like $LiLaTiO_4$ but also unusual anion ordering associated with the cation ordering: the *Ln* atoms form rock-salt layers with the S atoms and the Li atoms form antifluorite layers with the O2 atoms at 2*c*. The Ti atoms are surrounded by five oxygen atoms and one sulfur atom to form TiO_5S octahedra, which are corner-shared in the *ab* plane with each other via common O1 atoms. In Li*Ln*TiO_3S (*Ln* = La−Gd), The Ti−O1 bond distances in the *ab* plane (= 1.966−2.008 Å) are comparable to the sum of their ionic radii ($r(Ti^{4+})$ = 0.605 Å, $r(O^{2-})$ = 1.38 Å). In contrast, the Ti−O2 and Ti−S bond lengths along the *c*-axis change in opposite ways, compared with the ionic model ($r(S^{2-})$ = 1.84 Å): the Ti−O2 bond distances (= 1.750−1.766 Å) are approximately 11% shorter than that expected from the ionic model across all members while the Ti−S bond distances (= 2.856−2.865 Å) are approximately 15% longer.[38] As a result, the Ti atom is effectively shifted toward the apical oxygen in a square pyramidal configuration because of the covalent interactions between the Ti and O atoms and the steric effect caused by the large ionic radius of S^{2-}. This type of coordination geometry is observed in related Ti-based oxysulfides such as $LiLa_3Ti_2S_3O_6$[23] and $Ln_2Ti_2O_5S_2$.[39] The Li atoms are tetrahedrally coordinated with four oxygen atoms and edge-shared with each other via common O atoms. While the Li−O bond distances (= 2.045−2.028Å) in Li*Ln*TiO_3S are comparable to the sum of their ionic radii ($r(Li^+)$ = 0.59 Å),[38] the Li-centered tetrahedron is markedly compressed along the *c*-axis, yielding a flattened geometry characterized by a wide O2−Li−O2 angle (= 149.9−142.7°) in the *ab* plane. This tetrahedral distortion is likely attributed to tension from $(LnS)_2$ rock-salt layers with relatively large *Ln* and sulfide ions. It should be noted that the flatness of the perovskite layer, which is also associated with the $(LiO)_2$ antifluorite layer, stands in sharp contrast to the corrugated perovskite layers caused by the LiO_2S_2 tetrahedral chains in $LiLa_3Ti_2S_3O_6$.[23] The La atoms form monocapped square antiprisms, LaO_4S_5, which are connected by corner- or edge-sharing with common S and/or O atoms in the *ab* plane. Both the La−O and La−S bond lengths are comparable to the sum of their ionic radii.[38]

Figures 3 and 4 show the lattice parameters, unit cell volumes, and selected interatomic distances and angles of Li*Ln*TiO_3S plotted as a function of the Ln^{3+} ionic radius. The volume linearly decreased with decreasing ionic radius of Ln^{3+}, which is consistent with the monotonic decrease in all metal−ligand bond distances, except for the gradually expanding Ti−O2 bond distance. In contrast, the *a*- (*c*-) axis length contracted (expanded) as the ionic radius of *the* Ln^{3+} ions decreased. This behavior is different from that observed in Li*Ln*TiO_4, where the *a*- (*c*-) axis length conversely expanded (contracted) in the opposite direction owing to the TiO_6 octahedral rotations.[40] As shown in Figure S3, the elongation of the *c*-axis can be attributed not only to the increase in the Ti−O2 bond length, but also to the increase in the *c*-axis components of the Li−O2, Ti−O1, and *Ln*−S bond lengths, which accompanies the narrowing of the in-plane angles of O2−Li−O2, O1−Ti−O1, and S−*Ln*−S (Figure 4). In particular, the elongation of the Li−O2 bond length is as large as the change in the *c*-axis components of the *Ln*−O and *Ln*−S bond lengths that contract along the *c*-axis.

Bond valence sum (BVS) calculations[41] were performed to compare the oxidation numbers of the cations of Li*Ln*TiO_3S with their formal values (Table 1). The BVS values of the Li and Ti ions are somewhat lower than their formal valences across all members, suggesting an underbonded state for these metal cations, whereas the *Ln* ions appear overbonded. These behaviors result from a lattice mismatch between the $(LnS)_2$ rock-salt layers and Ti-based perovskite layers: the Ti−O1 bonds are stretched, and the *Ln*−S bonds are contracted compared to the sums of the corresponding ionic radii. Interestingly, the BVS values of Li, Ln, and Ti ions approach their respective formal valence values as the ionic radius of Ln^{3+} decreases, that is, the underbonded and overbonded states of these cations are gradually alleviated.

Solid State Reactions and Thermal Stability of Li*Ln*TiO_3S

Following the crystal growth results of Li*Ln*TiO_3S obtained by the flux method, we performed solid-state reactions using the starting materials described in the Experimental Section to synthesize polycrystalline samples. Figure 5 shows the representative powder XRD patterns of the products prepared at 900−1000 °C. As a result, only $LiNdTiO_3S$ was obtained as a pure phase, whereas the other *Ln* analogs always formed together with secondary phases, such as layered perovskite oxides or *Ln*-based oxysulfides. The cell parameters of Li*Ln*TiO_3S exhibited a linear dependence on the ionic radius of the Ln^{3+} ions, as observed in the corresponding single crystal samples (Figure S4). The TG curve of $LiNdTiO_3S$ shows high thermal stability in a flowing O_2 gas atmosphere up to 600 °C (Figure 6). The onset of the exothermic peaks observed in the DTA curve was concomitant with a gradual increase in the TG weight beginning just above 600 °C. An irreversible increase in TG weight was observed when the temperature exceeded 600

https://doi.org/10.1021/acs.chemmater.5c02924
Chem. Mater. 2026, 38, 1457−1468

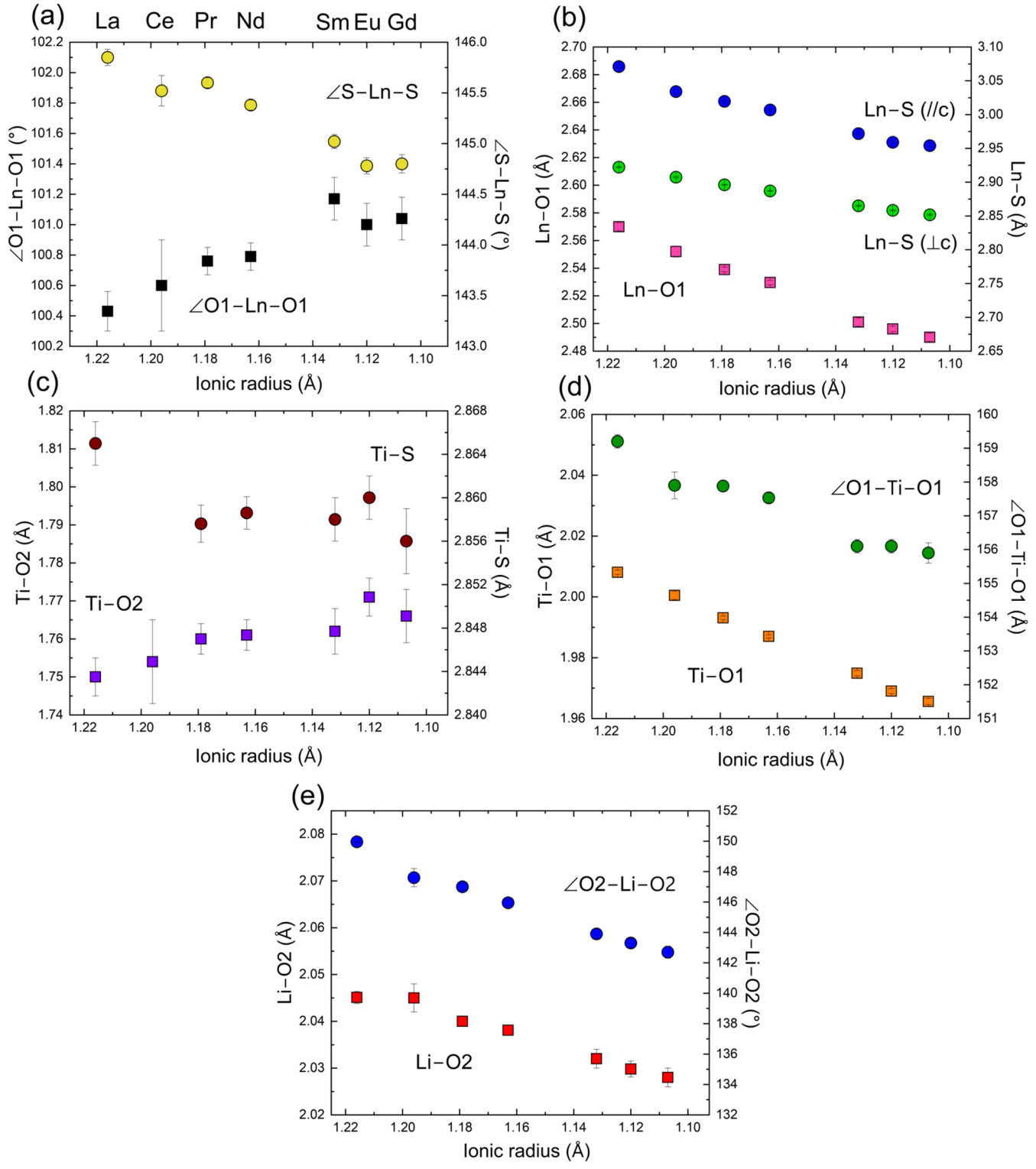

Figure 4. Selected interatomic distances and angles around metal centers plotted as a function of ionic radius of Ln^{3+}.

°C. The net weight gain was approximately 0.8%. Powder XRD analysis of $LiNdTiO_3S$ after the TG-DTA measurement revealed decomposition to $Nd_2Ti_2O_7$ (Figure S5). Given the TG weight gain, a sulfate like Li_2SO_4 might be formed during this decomposition process, although such a sulfate was not clearly observed in the XRD pattern, probably due to its amorphization and partial volatilization.

UV−vis−NIR Absorption Spectra

Figure 7 shows the UV−vis−NIR absorption spectra of the powdered $LiLnTiO_3S$ (Ln = La−Nd, Sm−Gd), which were obtained by converting the reflectance spectrum using the Kubelka−Munk transformation. The estimated bandgap is 2.45, 1.35, 2.23, 2.37, 2.34, 2.08, and 2.36 eV for Ln = La−Gd, respectively, which is consistent with the colors of the single crystal samples. These optical bandgap values were estimated by

https://doi.org/10.1021/acs.chemmater.5c02924
Chem. Mater. 2026, 38, 1457−1468

Table 1. Bond Valence Sum (BVS) Values of Li*Ln*TiO$_3$S (*Ln* = La, Ce, Pr, Nd, Sm, Eu, Gd)

	Li	*Ln*	Ti
LiLaTiO$_3$S	0.84	3.56	3.77
LiCeTiO$_3$S	0.84	3.52	3.78
LiPrTiO$_3$S	0.85	3.47	3.82
LiNdTiO$_3$S	0.85	3.39	3.88
LiSmTiO$_3$S	0.86	3.34	3.94
LiEuTiO$_3$S	0.87	3.25	3.95
LiGdTiO$_3$S	0.88	3.26	3.99

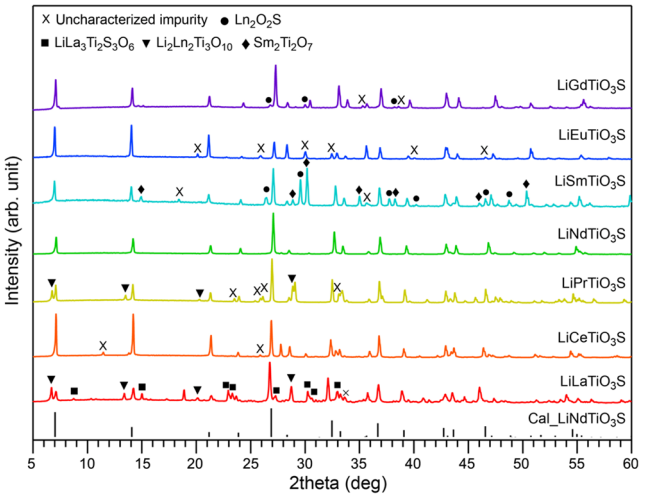

Figure 5. Powder XRD patterns of Li*Ln*TiO$_3$S synthesized by solid state reaction. For comparison, the powder XRD pattern of LiNdTiO$_3$S calculated based on the single crystal structure analysis is shown together.

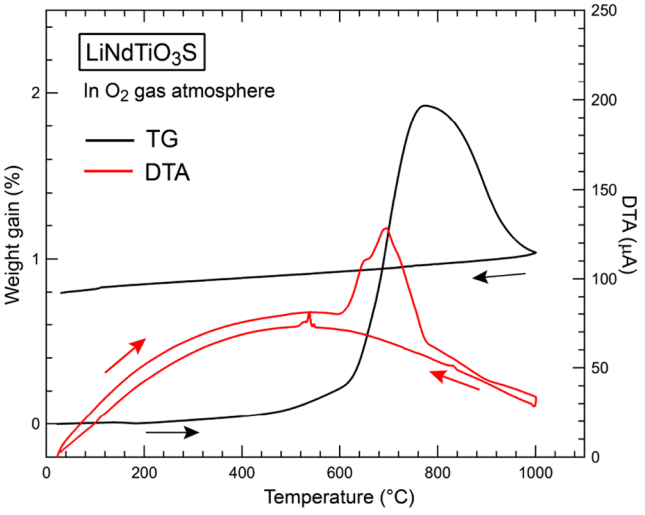

Figure 6. TG-DTA curves of LiNdTiO$_3$S under O$_2$ flow.

extrapolating the linear portion of the absorption curve to the baseline, except for *Ln* = Ce and Eu, in which weak absorption bands due to impurities appeared in the low-energy region. The small bandgap value for LiCeTiO$_3$S is ascribed to an optical transition from an f electronic state to the low-lying 3d state.[42] The observed small but sharp peaks for Pr and Nd are caused by f−f transitions of Ln^{3+} ions.[43,44] The bandgap values of Li*Ln*TiO$_3$S are even smaller than those of the corresponding oxides, that is, approximately 3.8 eV for Li*Ln*TiO$_4$ (*Ln* = La, Pr, Nd, Sm, Eu, Gd),[45,46] which can be rationalized by considering the high energy levels of the S 3p states, as discussed later.

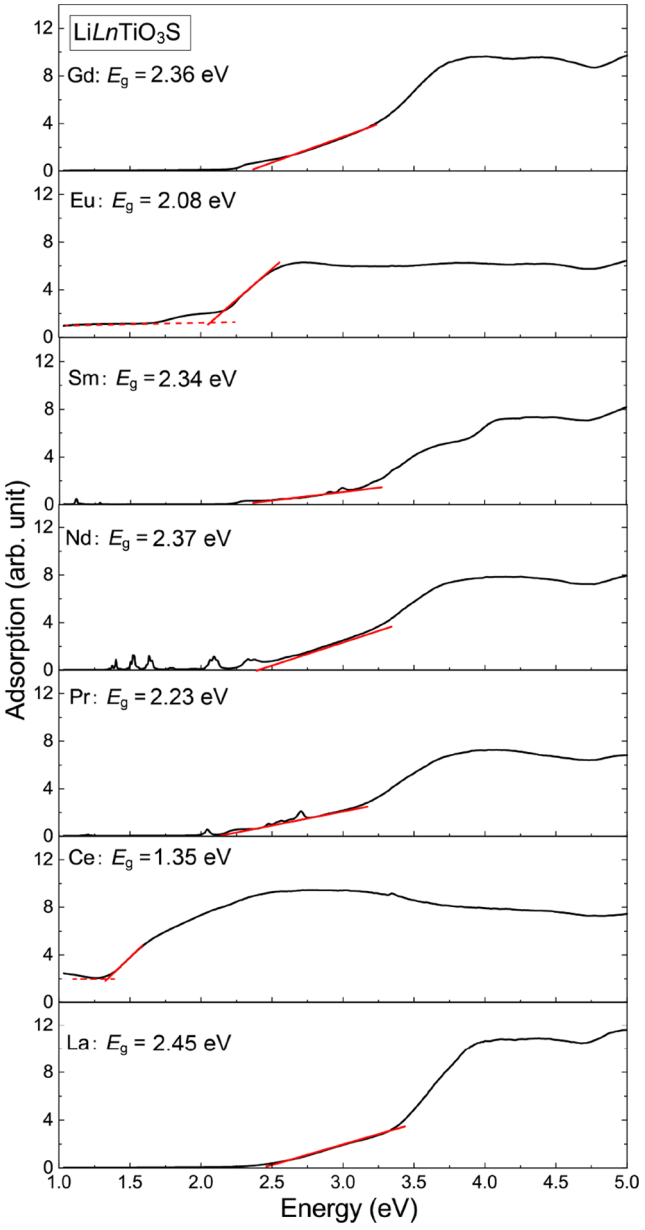

Figure 7. UV−vis−NIR absorption spectra of Li*Ln*TiO$_3$S, which were converted from the diffuse reflectance data using the Kubelka−Munk transformation. Solid and dashed lines stand for linear fitting lines and baselines, respectively.

DFT Calculations

First-principles calculations were performed to understand the electronic structure of Li*Ln*TiO$_3$S, particularly that of the nonmagnetic LiLaTiO$_3$S. The optimized lattice parameters and internal atomic positions of the relaxed unit cell obtained by the calculations were in good agreement with the refined crystallographic data. Figure 8 shows the band dispersion of LiLaTiO$_3$S. This indicates that LiLaTiO$_3$S has a direct-type bandgap energy of 1.14 eV at the Γ point. The bandgap energy is commonly underestimated in DFT calculations using the standard GGA. Figure 9 shows the total and partial density-of-states (DOS) plots. The S 3p band ranging from −3 eV to the Fermi energy (E_F) level dominates the valence band maximum (VBM),

https://doi.org/10.1021/acs.chemmater.5c02924
Chem. Mater. 2026, 38, 1457−1468

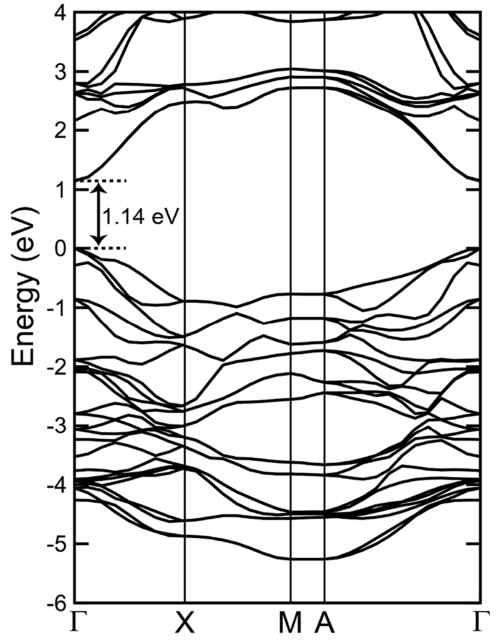

Figure 8. Electronic band dispersion curves of $LiLaTiO_3S$. The estimated energy gap at Γ is 1.14 eV.

followed by the O 2p band in the lower energy region, as often observed in oxysulfide compounds. The partial DOS plots also indicate that the Li 1s/2s orbitals are hybridized with the O 2p orbitals in the valence bands, which is in stark contrast to $LiLa_3Ti_2S_3O_6$,[23] where the Li 1s/2s orbitals are hybridized with both the O 2p and S 3p orbitals. The Ti 3d orbitals are strongly hybridized with the O 2p orbitals in the valence bands, while the interactions between Ti 3d and S 3p orbitals are rather weak. These results are consistent with the local coordination environment around the metal cations. The conduction band minimum (CBM) is primarily composed of the Ti 3d band. The electronic structure of $LiLaTiO_3S$ is similar to those of related layered titanium oxysulfides near the Fermi energy.[23,47]

Preparation of Nb-Doped $LiNdTiO_3S$

Since only $LiNdTiO_3S$ was obtained as a single phase by the solid-state reaction method, Nb atoms were doped into the Ti site to introduce Li-ion vacancies with the aim of inducing Li-ion conductivity. Figure S6a shows the PXRD patterns of $Li_{1-x}Nd(Ti_{1-x}Nb_x)O_3S$ (x = 0, 0.10, 0.20, 0.25, 0.30, 0.40), which were prepared by a solid-state reaction, as described in the Experimental Section. The x is the nominal Nb-doping concentration. While all doped phases could be obtained as a main phase in the range of $0 \le x \le 0.40$, a large number of impurity peaks, albeit with very low intensity, were observed in the doped phases with $x \ge 0.30$. Figure S6b,c show the lattice parameters and lattice volume, which were calculated by least-squares methods and plotted as a function of the Nb-doping concentration. While the a-axis length shows little change with increasing Nb doping (e.g., −0.3% between $0 \le x \le 0.25$), the c-axis length increases by 4.4% between $0 \le x \le 0.40$. In contrast, the unit cell volume, similar to the c-axis, increases with Nb content; however, for $x \ge 0.3$, both the volume and the c-axis length exhibit a reduced rate of increase. This suggests that Nb atoms are not properly incorporated at doping levels above x = 0.3, which is consistent with the enhanced impurity peaks observed in the XRD patterns. Ti-to-Nb substitution in

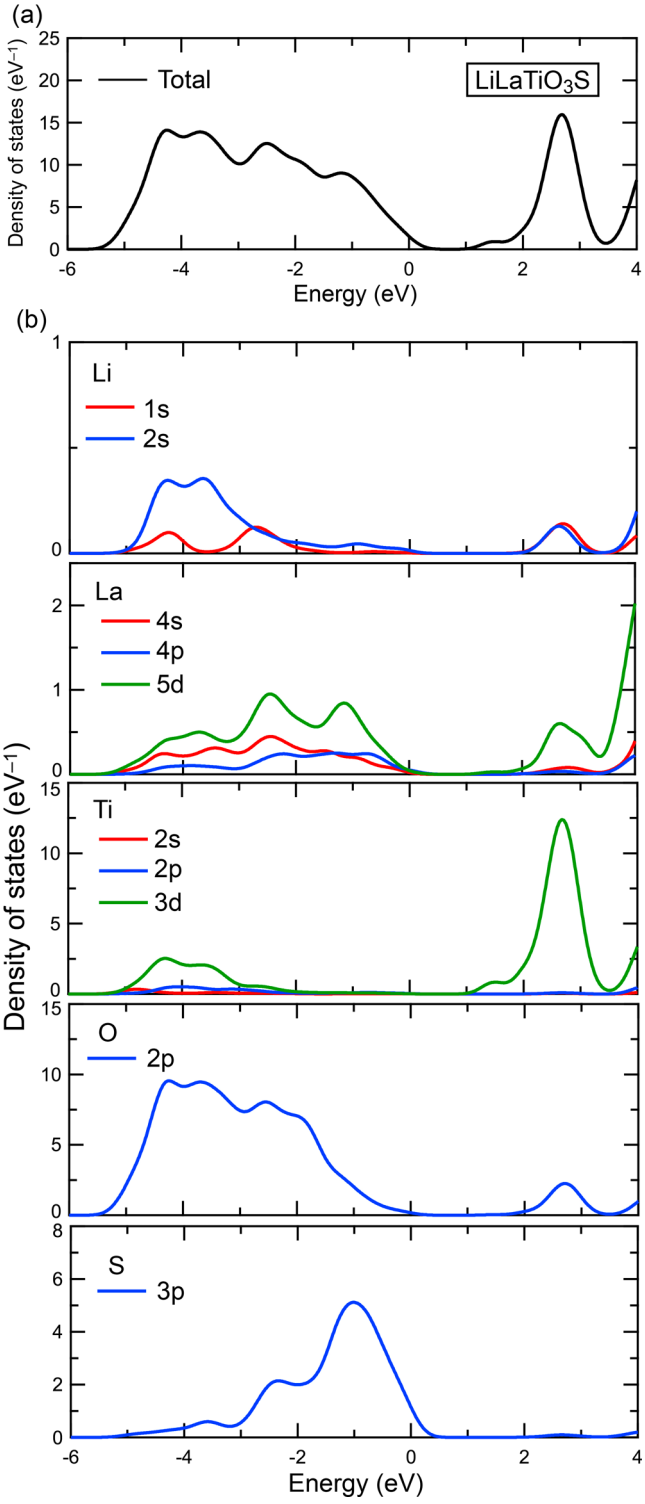

Figure 9. Total and partial density of states of $LiLaTiO_3S$ obtained by first-principles calculations.

$LiNdTiO_3S$ was confirmed by single-crystal structure analysis of the x = 0.10 sample (Tables S23−26).

Electrochemical Impedance Spectroscopy (EIS)

We investigated the ionic conductivity of $Li_{1-x}Nd(Ti_{1-x}Nb_x)O_3S$ (x = 0, 0.10, 0.20, 0.25) in the temperature range of 25−500 °C using electrochemical impedance spectroscopy (EIS). Figure 10(a) shows the Nyquist plots of the undoped phase in the temperature range of 100−500 °C. Figure 11 shows the

https://doi.org/10.1021/acs.chemmater.5c02924
Chem. Mater. 2026, 38, 1457−1468

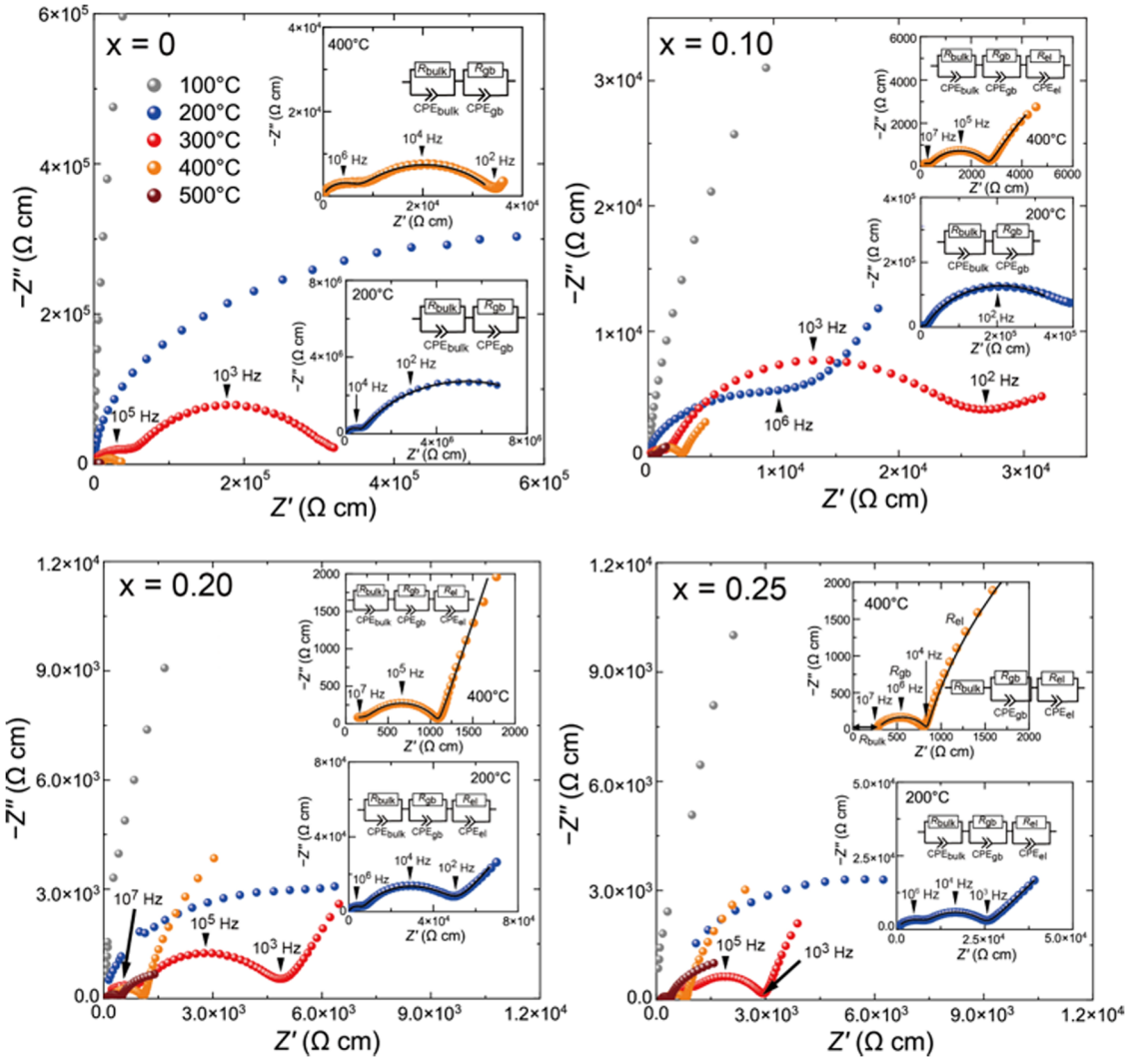

Figure 10. Nyquist plots of $Li_{1-x}Nd(Ti_{1-x}Nb_x)O_3S$ ($x = 0$, 0.10, 0.20, 0.25) recorded from 100 to 500 °C. Solid black lines in the plots at 200 and 400 °C are fitting ones calculated using (R_{bulk}−CPE_{bulk}, R_{gb}−CPE_{gb}), (R_{bulk}−CPE_{bulk}, R_{gb}−CPE_{gb}, R_{el}−CPE_{el}), or (R_{bulk}, R_{gb}−CPE_{gb}, R_{el}−CPE_{el}) circuit.

temperature dependences of the total (= bulk + grain boundary) conductivity (σ_{total}) and bulk conductivity (σ_{bulk}). Tables 2 and 3 present the values of σ_{total} and σ_{bulk}, and activation energies (E_a), respectively. The resistivity/conductivity was normalized by the dimensions of the sintered pellets. No semicircle associated with ionic conduction was observed in the $x = 0$ sample at room temperature; however, a semicircle that could be fitted using the total resistivity (R_{total}) and its corresponding constant phase element (CPE_{total}) appeared at 100 °C. Here, R_{total} and CPE_{total} represent the sum of the bulk resistivity (R_{bulk}) and grain-boundary resistivity (R_{gb}) and the sum of their corresponding constant phase elements, CPE_{bulk} and CPE_{gb}, respectively. Above 100 °C, the Nyquist plots could be resolved by an equivalent circuit model consisting of a series of two parallel components, (R_{bulk}−CPE_{bulk}, R_{gb}−CPE_{gb}), with an electrode-interface component (R_{el}−CPE_{el}) additionally included at high temperatures. The σ_{total} for $x = 0$ increases from 1.30×10^{-8} S cm^{-1} to 1.38×10^{-4} S cm^{-1} from 100 to 500 °C. In the measured temperature range, the σ_{total} of $LiNdTiO_3S$ is higher than those of $LiLnTiO_4$ (Ln = La, Nd) and $Li_2La_3Ti_3O_{10}$.[16,20] The E_a value of $x = 0$ is 0.641 eV, even lower than 0.83−0.84 eV for $LiLnTiO_4$ and 0.850 eV for $Li_2La_2Ti_3O_{10}$ but comparable to 0.693 eV for $Li_2Ca_2Ta_2TiO_{10}$.[20] The bulk conductivity of $LiNdTiO_3S$ is higher by approximately one to half an order of magnitude than the total conductivity in the range of $200 \leq T \leq 500$ °C.

The ionic conductivity of $LiNdTiO_3S$ is significantly improved by niobium doping. Figure S7 and Figure 10 show the Nyquist plots of the $x = 0.10$, 0.20, and 0.25 samples at 25 °C and temperatures from 100 to 500 °C, respectively, which can be basically fitted by three R-CPE in series, including (R_{el}−CPE_{el}) above 25 °C. Among the doped samples, the compositions with $x = 0.20$ and 0.25 exhibited similarly high ionic conductivities at 25 °C: $\sigma_{total} = 7.15 \times 10^{-9}$ S cm^{-1} and $\sigma_{bulk} = 3.00 \times 10^{-7}$ S cm^{-1} for $x = 0.20$ and $\sigma_{total} = 5.09 \times 10^{-9}$ S cm^{-1} and $\sigma_{bulk} = 3.00 \times 10^{-7}$ S cm^{-1} for $x = 0.25$; however, these values is still considerably lower than those of LLTO.[11] With increasing temperature, the bulk and grain-boundary components rapidly shrink, and a spike corresponding to the electrolyte−electrode interface component became distinct. The total conductivities of all doped samples at 500 °C reached values on the order of mS cm^{-1}, which are comparable to those of related layered perovskite oxides such as $Li_2LaTa_{1.2}Ti_{0.8}O_7$,[22] $Li_{1.75}La_2Ti_{2.75}Nb_{0.25}O_{10}$,[19] and $Li_{0.8}Sr_{0.8}La_{0.2}Nb_2O_7$[18] (Figure 11). In particular, the $x = 0.20$ sample at 500 °C exhibited the highest bulk conductivity of 1.46×10^{-2} S cm^{-1} among all Nb-doped samples, as well as any other RP-type oxide-based solid

https://doi.org/10.1021/acs.chemmater.5c02924
Chem. Mater. 2026, 38, 1457−1468

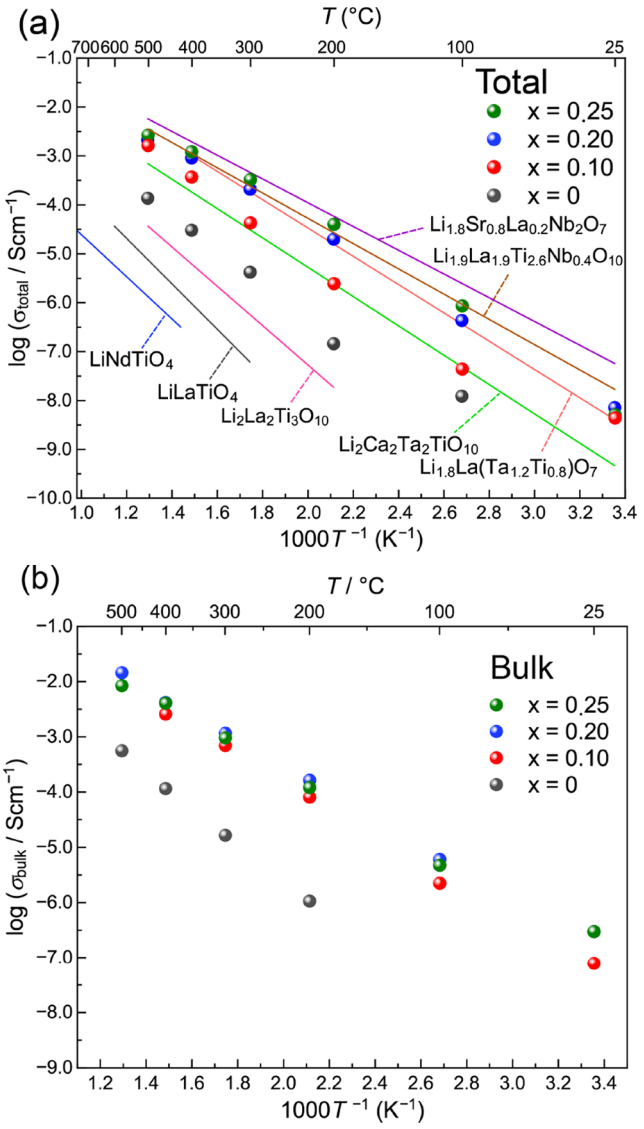

Figure 11. (a) Arrhenius plots of the total ionic conductivities of $Li_{1-x}Nd(Ti_{1-x}Nb_x)O_3S$ (x = 0, 0.10, 0.20, 0.25), compared with those of other layered lithium-ion conductors. (b) Arrhenius plots of the bulk ionic conductivities of $Li_{1-x}Nd(Ti_{1-x}Nb_x)O_3S$. Estimated activation energies for σ_{bulk} and σ_{total} are summarized in Table 3.

electrolytes. The x = 0.20 and 0.25 samples exhibit similarly low activation energies for conductivity, with 0.579 and 0.596 eV corresponding to their total conductivities and 0.495 and 0.485 eV corresponding to their bulk conductivities, respectively. This result indicates that the mobile Li-ion carrier concentration does not scale with lithium-ion deficiency between x = 0.20 and 0.25.

Table 3. Activation Energy E_a (eV) of $Li_{1-x}Nd(Ti_{1-x}Nb_x)O_3S$ (x = 0, 0.10, 0.20, 0.25)

compound	E_a (bulk)	E_a (total)
x = 0	0.715	0.641
x = 0.10	0.523	0.594
x = 0.20	0.495	0.579
x = 0.25	0.485	0.596

Notably, $LiNdTiO_3S$ is the first RP-type oxide-based lithium-ion conductor in which a bulk component has been observed. The corresponding activation energies, particularly for the x = 0.20 and 0.25 samples, are significantly lower than the lowest value (0.57 eV) reported for $Li_2LaTa_{1.2}Ti_{0.8}O_7$.[22] However, these values are still greater than those (0.3−0.4 eV) of LLTO above room temperature.[11,12]

DISCUSSION

A series of $LiLnTiO_3S$ (Ln = La−Nd, Sm−Gd) compounds were successfully synthesized using the flux methods and solid state reactions. Unlike $LiLnTiO_4$, an ion-exchange process is not necessary. A comparison with $LiLa_3Ti_2S_3O_6$ with corrugated perovskite-like layers shows that a coordination change from LiO_2S_2 to LiO_4 tetrahedra stabilizes the flat perovskite layer in $LiLnTiO_3S$. The oxysulfide maintains the space group $P4/nmm$ from La to Gd, which stands in contrast to the related oxide $LiLnTiO_4$, where the structural symmetry lowers to $P\text{-}42_1m$ between Nd and Sm.[48] In fact, calculations of the phonon band structures for $LiLaTiO_3S$ and $LiGdTiO_3S$ revealed no unstable modes (Figure S8). In oxides, even in $ALnTiO_4$ (A = Na, K, Ag) compounds with larger ionic sizes than Li, $P\text{-}42_1m$ becomes stabilized as the ionic radius of Ln decreases.[40,49,50] In contrast, the substitution of the apical anion sites with sulfide ions strongly suppresses the rotation of the oxygen octahedra, which may be attributed to steric effects or Coulomb repulsion between the sulfide ions.

The EIS measurements for $LiNdTiO_3S$ revealed a significant enhancement in ionic conductivity by Nb doping, which has not been confirmed in the corresponding layered oxide $LiLnTiO_4$. In contrast to other related layered titanium oxides, bulk conductivity components were observed exclusively in $LiNdTiO_3S$, which exhibited the highest lithium-ion mobility. To understand the lithium-ion conduction pathways in $LiNdTiO_3S$, the BVE calculations were performed using the crystal structure determined by the single crystal structure analysis. Figure S9 shows the BVE landscape for a Li^+ ion in $LiNdTiO_3S$ at the isosurface level of 1.0 eV, which clearly visualizes 2D conduction pathways between Li^+ sites in the antifluorite layers. The calculated BVE barriers for Li^+ migration are 0.532 eV along the a and b axes, which is close to the experimental activation energy values. It is no doubt that the observed enhanced conductivity

Table 2. Variable Temperature Conductivity (S cm^{-1}) of $Li_{1-x}Nd(Ti_{1-x}Nb_x)O_3S$ (x = 0, 0.10, 0.20, 0.25)

	x = 0		x = 0.10		x = 0.20		x = 0.25	
compound	bulk	total	bulk	total	bulk	total	bulk	total
25 °C	N/A	N/A	7.88×10^{-8}	4.38×10^{-9}	3.00×10^{-7}	7.15×10^{-9}	3.00×10^{-7}	5.09×10^{-9}
100 °C	N/A	1.30×10^{-8}	2.24×10^{-6}	4.37×10^{-8}	6.02×10^{-6}	4.31×10^{-7}	4.70×10^{-6}	8.69×10^{-7}
200 °C	1.06×10^{-6}	1.45×10^{-7}	8.15×10^{-5}	2.43×10^{-6}	1.64×10^{-4}	2.00×10^{-5}	1.21×10^{-4}	4.02×10^{-5}
300 °C	1.66×10^{-5}	4.20×10^{-6}	7.01×10^{-4}	4.25×10^{-5}	1.16×10^{-3}	2.07×10^{-4}	9.54×10^{-4}	3.30×10^{-4}
400 °C	1.15×10^{-4}	3.02×10^{-5}	2.60×10^{-3}	3.70×10^{-4}	4.18×10^{-3}	9.07×10^{-4}	4.07×10^{-3}	1.22×10^{-3}
500 °C	5.64×10^{-4}	1.38×10^{-4}	5.88×10^{-3}	1.62×10^{-3}	1.46×10^{-2}	2.12×10^{-3}	8.53×10^{-3}	2.68×10^{-3}

https://doi.org/10.1021/acs.chemmater.5c02924
Chem. Mater. 2026, 38, 1457−1468

can be attributed to the lithium site vacancies in the antifluorite layers via the substitution of Nb^{5+} ions for Ti^{4+} ions.[22,51] Bulk ionic conductivity has not been observed in other related layered ion conductors, rendering direct comparative analysis of the origin of the high lithium-ion mobility in $LiNdTiO_3S$ challenging. While short Li−Li interatomic distances have been proposed to contribute to enhanced ionic conductivity in certain layered materials, a trend has emerged in which compounds with longer Li−Li interatomic distances tend to exhibit higher conductivities. For instance, although the Li−Li interatomic distance in $LiNdTiO_3S$ is greater than that in $LiLnTiO_4$ (Ln = La, Nd),[48] the total conductivity of $LiNdTiO_3S$ surpasses those of $LiLnTiO_4$. Similarly, $LiSr_2Nb_2O_7$, which exhibits the highest total conductivity by La doping among analogous layered oxides,[18] possesses longer Li−Li interatomic distances than $LiNdTiO_3S$. These extended Li−Li interatomic distances are inferred to induce an underbonded environment around the lithium atoms, as suggested by the BVS values of $LiLnTiO_3S$, thereby facilitating lithium-ion migration. However, other factors, such as lithium vacancy concentration, grain boundary dimensions, and interfacial contact must also be considered, as they exert a significant influence on the observed conductivity. Further theoretical approaches, including molecular dynamics simulations, are essential for comprehensively understanding ion migration mechanisms at the microscopic level.

CONCLUSIONS

In summary, the n = 1 Ruddlesden−Popper type titanium oxysulfide compounds, $LiLnTiO_3S$ (Ln = La, Ce, Pr, Nd, Sm, Eu, Gd), were successfully synthesized by the flux method using molten chloride salts. These crystal structures adopted a centrosymmetric tetragonal cell in contrast to the corresponding oxides $LiLnTiO_4$ involving inversion symmetry breaking. UV−vis−NIR absorption measurements on $LiLnTiO_3S$ revealed the bandgaps between 2.08−2.37 eV, except for Ln = Ce. First-principles calculations of Ln = La indicated that the conduction band minimum was composed of Ti-3d orbitals, while the valence band maximum was composed of both O 2p and S 3p orbitals. The ionic conductivity of $LiNdTiO_3S$ was significantly enhanced by aliovalent doping with niobium, which resulted in the formation of lithium-ion vacancies in the $(LiO)_2$ antifluorite layers. $LiNdTiO_3S$ was the first RP-type oxide-based solid electrolyte in which bulk ionic conductivity was observed, with notably higher values at x = 0.20 and 0.25. $LiLnTiO_3S$ is expected to serve as an ideal model material for further understanding the ion conduction phenomena in 2D antifluorite layers and facilitate the advancement of novel lithium-ion conductors utilizing mixed anions. Large-scale single-crystal growth of $LiLnTiO_3S$ is under investigation to assess ionic conductivity anisotropy. Very recently, a sodium-containing analogue, $NaMTiO_{2.2}S_{1.8}$ (M = Nd, Sm), was synthesized by Abe et al., and its visible-light-responsive photocatalytic properties were reported.[52] This sodium analogue was obtained by heating $NaMTiO_4$ under a flowing H_2S atmosphere. In contrast to the title compound, it exhibits a higher degree of substitution of sulfide ions for oxide ions and, moreover, forms Na(S/O) rock-salt layers. The exploration of the ionic conductivity of $NaMTiO_{2.2}S_{1.8}$ and the photocatalytic properties of $LiLnTiO_3S$ is expected to deepen the understanding of oxysulfide chemistry.

ASSOCIATED CONTENT

Supporting Information

The Supporting Information is available free of charge at https://pubs.acs.org/doi/10.1021/acs.chemmater.5c02924.

EDX spectra, single crystal XRD data, refined crystallographic data, anisotropic displacement parameters, selected bond distances and angles for $LiLnTiO_3S$ (Ln = La−Nd, Sm−Gd) and $Li_{0.9}Nd(Ti_{0.9}Nb_{0.1})O_3S$. SEM images, powder XRD patterns, lattice parameters and volume of $LiLnTiO_3S$ and Nb-doped $LiNdTiO_3S$, powder XRD pattern of $LiNdTiO_3S$ after TG-DTA measurements, typical Nyquist plots of Nb-doped $LiNdTiO_3S$ at room temperature, and calculated phonon band structures of $LiLnTiO_3S$ (Ln = La, Gd) (PDF)

Accession Codes

Deposition Numbers 2498335−2498340 and 2498515−2498516 contain the supplementary crystallographic data for this paper. These data can be obtained free of charge via the joint Cambridge Crystallographic Data Centre (CCDC) and Fachinformationszentrum Karlsruhe Access Structures service.

AUTHOR INFORMATION

Corresponding Authors

Naoaki Kuwata − *Graduate School of Chemical Sciences and Engineering, Hokkaido University, Sapporo, Hokkaido 060-0810, Japan; Center for Green Research on Energy and Environmental Materials, NIMS, Tsukuba, Ibaraki 305-0044, Japan;* orcid.org/0000-0002-0736-6967; Email: KUWATA.Naoaki@nims.go.jp

Yoshihiro Tsujimoto − *Research Center for Materials Nanoarchitechtonics (MANA), National Institute for Materials Science (NIMS), Tsukuba, Ibaraki 305-0044, Japan; Graduate School of Chemical Sciences and Engineering, Hokkaido University, Sapporo, Hokkaido 060-0810, Japan;* orcid.org/0000-0003-2140-3362; Email: TSUJIMOTO.Yoshihiro@nims.go.jp

Authors

Hongbo Yuan − *Research Center for Materials Nanoarchitechtonics (MANA), National Institute for Materials Science (NIMS), Tsukuba, Ibaraki 305-0044, Japan; Graduate School of Chemical Sciences and Engineering, Hokkaido University, Sapporo, Hokkaido 060-0810, Japan*

Kaori Sugii − *Center for Green Research on Energy and Environmental Materials, NIMS, Tsukuba, Ibaraki 305-0044, Japan*

Gen Hasegawa − *Center for Green Research on Energy and Environmental Materials, NIMS, Tsukuba, Ibaraki 305-0044, Japan;* orcid.org/0000-0002-9297-6902

Yu Meng − *Research Center for Materials Nanoarchitechtonics (MANA), National Institute for Materials Science (NIMS), Tsukuba, Ibaraki 305-0044, Japan; Graduate School of Chemical Sciences and Engineering, Hokkaido University, Sapporo, Hokkaido 060-0810, Japan*

Yoshitaka Matsushita − *Surface and Bulk Analysis Unit, NIMS, Tsukuba, Ibaraki 305-0047, Japan;* orcid.org/0000-0002-4968-8905

Hirofumi Akamatsu − *Department of Applied Chemistry, Kyushu University, Fukuoka 819-0395, Japan;* orcid.org/0000-0003-2867-2127

Kazunari Yamaura − *Research Center for Materials Nanoarchitechtonics (MANA), National Institute for Materials Science (NIMS), Tsukuba, Ibaraki 305-0044, Japan; Graduate School of Chemical Sciences and Engineering, Hokkaido University, Sapporo, Hokkaido 060-0810, Japan;* orcid.org/0000-0003-0390-8244

Complete contact information is available at: https://pubs.acs.org/10.1021/acs.chemmater.5c02924

Author Contributions

The manuscript was written through contributions of all authors. All authors have given approval to the final version of the manuscript.

Notes

The authors declare no competing financial interest.

■ ACKNOWLEDGMENTS

This study was partly supported by the World Premier International Research Center Initiative (WPI), the JSPS KAKENHI (grant no. 25K01507, 25K01657). Y.T. acknowledges the grant from the Iketani Science and Technology Foundation and the Kazuchika Okura Memorial Foundation.

■ REFERENCES

(1) Lu, D.; Shao, Y.; Lozano, T.; Bennett, W. D.; Graff, G. L.; Polzin, B.; Zhang, J.; Engelhard, M. H.; Saenz, N. T.; Henderson, W. A.; Bhattacharya, P.; Liu, J.; Xiao, J. Failure Mechanism for Fast-Charged Lithium Metal Batteries with Liquid Electrolytes. *Adv. Energy. Mater.* **2015**, *5*, No. 1400993.

(2) Gao, Z.; Sun, H.; Fu, L.; Ye, F.; Zhang, Y.; Luo, W.; Huang, Y. Promises, Challenges, and Recent Progress of Inorganic Solid-State Electrolytes for All-Solid-State Lithium Batteries. *Adv. Mater.* **2018**, *30*, No. 1705702.

(3) Famprikis, T.; Canepa, P.; Dawson, J. A.; Islam, M. S.; Masquelier, C. Fundamentals of Inorganic Solid-State Electrolytes for Batteries. *Nat. Mater.* **2019**, *18*, 1278−1291.

(4) Kamaya, N.; Homma, K.; Yamakawa, Y.; Hirayama, M.; Kanno, R.; Yonemura, M.; Kamiyama, T.; Kato, Y.; Hama, S.; Kawamoto, K.; Mitsui, A. A Lithium Superionic Conductor. *Nat. Mater.* **2011**, *10*, 682−686.

(5) Seino, Y.; Ota, T.; Takada, K.; Hayashi, A.; Tatsumisago, M. A Sulphide Lithium Super Ion Conductor Is Superior to Liquid Ion Conductors for Use in Rechargeable Batteries. *Energy Environ. Sci.* **2014**, *7*, 627−631.

(6) Kanno, R.; Murayama, M. Lithium Ionic Conductor Thio-LISICON: The Li_2S-GeS_2-P_2S_5 System. *J. Electrochem. Soc.* **2001**, *148*, No. A742.

(7) Aimi, A.; Onodera, H.; Shimonishi, Y.; Fujimoto, K.; Yoshida, S. High Li-Ion Conductivity in Pyrochlore-Type Solid Electrolyte $Li_{2-x}La_{(1+x)/3}M_2O_6F$ (M = Nb, Ta). *Chem. Mater.* **2024**, *36*, 3717−3725.

(8) Kim, J.; Kim, J.; Avdeev, M.; Yun, H.; Kim, S. J. $LiTa_2PO_8$: A Fast Lithium-Ion Conductor with New Framework Structure. *J. Mater. Chem. A* **2018**, *6*, 22478−22482.

(9) Murugan, R.; Thangadurai, V.; Weppner, W. Fast Lithium Ion Conduction in Garnet-Type $Li_7La_3Zr_2O_{12}$. *Angew. Chem., Int. Ed.* **2007**, *46*, 7778−7781.

(10) Arbi, K.; Rojo, J. M.; Sanz, J. Lithium Mobility in Titanium Based Nasicon $Li_{1+x}Ti_{2-x}Al_x(PO_4)_3$ and $LiTi_{2-x}Zr_x(PO_4)_3$ Materials Followed by NMR and Impedance Spectroscopy. *J. Eur. Ceram. Soc.* **2007**, *27*, 4215−4218.

(11) Inaguma, Y.; Liquan, C.; Itoh, M.; Nakamura, T.; Uchida, T.; Ikuta, H.; Wakihara, M. High Ionic Conductivity in Lithium Lanthanum Titanate. *Solid State Commun.* **1993**, *86*, 689−693.

(12) Kobayashi, S.; Yokoe, D.; Fujiwara, Y.; Kawahara, K.; Ikuhara, Y.; Kuwabara, A. Lithium Lanthanum Titanate Single Crystals: Dependence of Lithium-Ion Conductivity on Crystal Domain Orientation. *Nano Lett.* **2022**, *22*, 5516−5522.

(13) Catti, M. Short-Range Order and Li+ Ion Diffusion Mechanisms in $Li_5La_9\square_2(TiO_3)_{16}$ (LLTO). *Solid State Ion.* **2011**, *183*, 1−6.

(14) Moriwake, H.; Gao, X.; Kuwabara, A.; Fisher, C. A. J.; Kimura, T.; Ikuhara, Y. H.; Kohama, K.; Tojigamori, T.; Ikuhara, Y. Domain Boundaries and Their Influence on Li Migration in Solid-State Electrolyte $(La,Li)TiO_3$. *J. Power Sources* **2015**, *276*, 203−207.

(15) Hasegawa, G.; Kuwata, N.; Ohnishi, T.; Takada, K. Visualization and Evaluation of Lithium Diffusion at Grain Boundaries in $Li_{0.29}La_{0.57}TiO_3$ Solid Electrolytes Using Secondary Ion Mass Spectrometry. *J. Mater. Chem. A* **2024**, *12*, 731−738.

(16) Thangadurai, V.; Shukla, A. K.; Gopalakrishnan, J.; Joubert, O.; Brohan, L.; Tournoux, M. X-Ray Powder Diffraction Study of $LiLnTiO_4$ (Ln = La,Nd): A Lithium-Ion Conductor. *Mater. Sci. Forum* **2000**, *321*−*324*, 965−970.

(17) TODA, K.; KURITA, S.; SATO, M. New Layered Perovskite Compounds, $LiLaTiO_4$ and $LiEuTiO_4$. *J. Ceram. Soc. Jpn.* **1996**, *104*, 140−142.

(18) Fanah, S. J.; Ramezanipour, F. Enhancing the Lithium-Ion Conductivity in $Li_2SrTa_{2-x}Nb_xO_7$ (x = 0−2). *Solid State Sci.* **2019**, *97*, No. 106014.

(19) Fanah, S. J.; Ramezanipour, F. Strategies for Enhancing Lithium-Ion Conductivity of Triple-Layered Ruddlesden-Popper Oxides: Case Study of $Li_{2-x}La_{2-y}Ti_{3-z}Nb_zO_{10}$. *Inorg. Chem.* **2020**, *59*, 9718−9727.

(20) Fanah, S. J.; Ramezanipour, F. Symmetry Effect on the Enhancement of Lithium-Ion Mobility in Layered Oxides $Li_2A_2B_2TiO_{10}$ (A = La, Sr, Ca; B = Ti, Ta). *J. Phys. Chem. C* **2021**, *125*, 3689−3697.

(21) Fanah, S. J.; Yu, M.; Ramezanipour, F. Experimental and Theoretical Investigation of Lithium-Ion Conductivity in $Li_2LaNbTiO_7$. *Dalton Trans.* **2019**, *48*, 17281−17290.

(22) Fanah, S. J.; Yu, M.; Huq, A.; Ramezanipour, F. Insight into Lithium-Ion Mobility in $Li_2La(TaTi)O_7$. *J. Mater. Chem. A* **2018**, *6*, 22152−22160.

(23) Yuan, H.; Yan, H.; Meng, Y.; Matsushita, Y.; Yamaura, K.; Tsujimoto, Y. Flux Crystal Growth, Structure, and Optical Properties of $LiLa_3Ti_2S_3O_6$: An Oxysulfide Phase Derived from K2NiF4-Type Structure. *Inorg. Chem.* **2024**, *63*, 15443−15450.

(24) Adachi, G. Y.; Imanaka, N.; Tamura, S.; Gupta, A. S.; Akamatsu, H.; Strayer, M. E.; Lei, S.; Kuge, T.; Fujita, K.; dela Cruz, C.; Togo, A.; Tanaka, I.; Tanaka, K.; Mallouk, T. E.; Gopalan, V.; Evans, H. A.; Mao, L.; Seshadri, R.; Cheetham, A. K.; Aluminum, L.; Phosphate, T.; Titanate, L. L.; Lanthanum, A. L.; Oxide, Z. Improper Inversion Symmetry Breaking and Piezoelectricity through Oxygen Octahedral Rotations in Layered Perovskite Family, $LiRTiO_4$ (R = Rare Earths). *Annu. Rev. Mater. Res.* **2002**, *51*, 351−380.

(25) Sheldrick, G. M. SHELXT - Integrated Space-Group and Crystal-Structure Determination. *Acta Crystallogr. A* **2015**, *71*, 3−8.

(26) Sheldrick, G. M. Crystal Structure Refinement with SHELXL. *Acta Crystallogr. C* **2015**, *71*, 3−8.

(27) Dolomanov, O. V.; Blake, A. J.; Champness, N. R.; Schröder, M. OLEX: New Software for Visualization and Analysis of Extended Crystal Structures. *J. Appl. Crystallogr.* **2003**, *36*, 1283−1284.

(28) Clark, S. J.; Segall, M. D.; Pickard, C. J.; Hasnip, P. J.; Probert, M. I. J.; Refson, K.; Payne, M. C. First Principles Methods Using CASTEP. *Z. Kristallogr. - Cryst. Mater.* **2005**, *220*, 567−570.

(29) Togo, A. First-Principles Phonon Calculations with Phonopy and Phono3py. *J. Phys. Soc. Jpn.* **2023**, *92*, No. 012001.

(30) Togo, A.; Chaput, L.; Tadano, T.; Tanaka, I. Implementation Strategies in Phonopy and Phono3py. *J. Phys.: Cond. Matter* **2023**, *35*, No. 353001.

(31) Kresse, G.; Hafner, J. Ab Initio Molecular Dynamics for Open-Shell Transition Metals. *Phys. Rev. B* **1993**, *48*, No. 13115.

(32) Kresse, G.; Furthmüller, J. Efficient Iterative Schemes for Ab Initio Total-Energy Calculations Using a Plane-Wave Basis Set. *Phys. Rev. B* **1996**, *54*, No. 11169.

(33) M Ganose, A.; J Jackson, A.; O Scanlon, D. Sumo: Command-Line Tools for Plotting and Analysis of Periodic Ab Initio Calculations. *J. Open Source Softw.* **2018**, *3*, No. 717.
(34) Sale, M.; Avdeev, M. 3DBVSMAPPER: A Program for Automatically Generating Bond-Valence Sum Landscapes. *J. Appl. Crystallogr.* **2012**, *45*, 1054−1056.
(35) Adams, S. Modelling Ion Conduction Pathways by Bond Valence Pseudopotential Maps. *Solid State Ion.* **2000**, *136*−*137*, 1351−1361.
(36) Chen, H.; Wong, L. L.; Adams, S. SoftBV− a Software Tool for Screening the Materials Genome of Inorganic Fast Ion Conductors. *Acta Crystallogr. B* **2019**, *75*, 18−33.
(37) Momma, K.; Izumi, F. VESTA3 for Three-Dimensional Visualization of Crystal, Volumetric and Morphology Data. *J. Appl. Crystallogr.* **2011**, *44*, 1272−1276.
(38) Shannon, R. D. Revised Effective Ionic Radii and Systematic Studies of Interatomic Distances in Halides and Chalcogenides. *Acta Crystallogr. A* **1976**, *32*, 751−767.
(39) Goga, M.; Seshadri, R.; Ksenofontov, V.; Gütlich, P.; Tremel, W. $Ln_2Ti_2S_2O_5$ (Ln = Nd, Pr, Sm): A Novel Series of Defective Ruddlesden−Popper Phases. *Chem. Commun.* **1999**, *11*, 979−980.
(40) Akamatsu, H.; Fujita, K.; Kuge, T.; Gupta, A. S.; Togo, A.; Lei, S.; Xue, F.; Stone, G.; Rondinelli, J. M.; Chen, L. Q.; Tanaka, I.; Gopalan, V.; Tanaka, K. Inversion Symmetry Breaking by Oxygen Octahedral Rotations in the Ruddlesden-Popper $NaRTiO_4$ Family. *Phys. Rev. Lett.* **2014**, *112*, 1−5.
(41) Brese, N. E.; O'Keeffe, M. Bond-Valence Parameters for Solids. *Acta Crystallogr. B* **1991**, *47*, 192−197.
(42) Ueda, J.; Tanabe, S. Review of Luminescent Properties of Ce^{3+}-Doped Garnet Phosphors: New Insight into the Effect of Crystal and Electronic Structure. *Opt. Mater.:X* **2019**, *1*, No. 100018.
(43) Du, Q.; Ueda, J.; Tanabe, S. Toward Color Variation of Long Persistent Luminescence in Pr^{3+}-Doped Garnet Transparent Ceramic Phosphors. *J. Mater. Chem. C* **2023**, *11*, 16225−16233.
(44) Back, M.; Xu, J.; Ueda, J.; Benedetti, A.; Tanabe, S. Thermochromic Narrow Band Gap Phosphors for Multimodal Optical Thermometry: The Case of Y^{3+}-Stabilized β-Bi_2O_3:Nd^{3+}. *Chem. Mater.* **2022**, *34*, 8198−8206.
(45) Song, S.-H. Eu^{3+} /Eu^{2+} Redox Energy in a New Lithium Intercalation Compound $Li_xEuTa_7O_{19}$ ($0 \leq x \leq 1$). *J. Solid State Electrochem.* **2021**, *25*, 1−7.
(46) Song, S.-H.; Ahn, K.; Kanatzidis, M. G.; Alonso, J. A.; Cheng, J.-G.; Goodenough, J. B. Effect of an Internal Electric Field on the Redox Energies of $ALnTiO_4$ (A = Na or Li, Ln = Y or Rare-Earth). *Chem. Mater.* **2013**, *25*, 3852−3857.
(47) Brlec, K.; Savory, C. N.; Scanlon, D. O. Understanding the Electronic Structure of $Y_2Ti_2O_5S_2$ for Green Hydrogen Production: A Hybrid-DFT and GW Study. *J. Mater. Chem. A* **2023**, *11*, 16776−16787.
(48) Gupta, A. S.; Akamatsu, H.; Strayer, M. E.; Lei, S.; Kuge, T.; Fujita, K.; dela Cruz, C.; Togo, A.; Tanaka, I.; Tanaka, K.; Mallouk, T. E.; Gopalan, V. Improper Inversion Symmetry Breaking and Piezoelectricity through Oxygen Octahedral Rotations in Layered Perovskite Family, $LiRTiO_4$ (R = Rare Earths). *Adv. Electron. Mater.* **2016**, *2*, No. 1500196.
(49) Yoshida, S.; Akamatsu, H.; Gibbs, A. S.; Kawaguchi, S.; Gopalan, V.; Tanaka, K.; Fujita, K. Interplay between Oxygen Octahedral Rotation and Deformation in the Acentric $ARTiO_4$ Series toward Negative Thermal Expansion. *Chem. Mater.* **2022**, *34*, 6492−6504.
(50) Akamatsu, H.; Fujita, K.; Kuge, T.; Gupta, A. S.; Rondinelli, J. M.; Tanaka, I.; Tanaka, K.; Gopalan, V. A -Site Cation Size Effect on Oxygen Octahedral Rotations in Acentric Ruddlesden-Popper Alkali Rare-Earth Titanates. *Phys. Rev. Mater.* **2019**, *3*, 1−10.
(51) Ramakrishnan, P.; Kwak, H.; Cho, Y. H.; Kim, J. H. Ionic Conductivity of Ruddlesden-Popper Layered Perovskites ($Li_2SrTa_2O_7$, $Li_2SrNb_2O_7$, and $Li_2CaTa_2O_7$) with Poly (Ethylene Oxide) as a Composite Solid Electrolyte. *ChemElectroChem* **2018**, *5*, 1265−1271.
(52) Ishii, Y.; Suzuki, H.; Kato, D.; Tomita, O.; Nakada, A.; Abe, R. Interlayer-Active Layered Oxysulfides $NaMTiO_{2.2}S_{1.8}$ (M = Nd, Sm) with an n = 1 Ruddlesden−Popper Structure Acting as Photocatalysts for Visible Light Water Splitting. *Chem. Sci.* **2025**, *16*, 16534−16541.

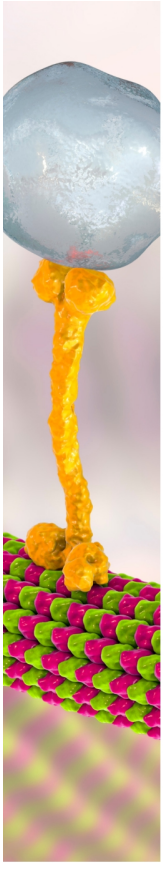

https://doi.org/10.1021/acs.chemmater.5c02924
Chem. Mater. 2026, 38, 1457−1468